Beyond the lowest Landau level: Unlocking more robust fractional states using flat Chern bands with higher vortexability

Yitong Zhang,[1,*] Siddhartha Sarkar,[2,*] Xiaohan Wan,[1,3,*] Daniel E. Parker,[4,†] Shi-Zeng Lin,[5,6,‡] and Kai Sun[1,§]

[1]*Department of Physics, University of Michigan, Ann Arbor, Michigan 48109, USA*

[2]*Max Planck Institute for the Physics of Complex Systems, Nöthnitzer Straße 38, 01187 Dresden, Germany*

[3]*Department of Physics, University of Washington, Seattle, Washington 98195, USA*

[4]*Department of Physics, University of California at San Diego, La Jolla, California 92093, USA*

[5]*Theoretical Division, T-4 and CNLS, Los Alamos National Laboratory, Los Alamos, New Mexico 87545, USA*

[6]*Center for Integrated Nanotechnologies (CINT), Los Alamos National Laboratory, Los Alamos, New Mexico 87545, USA*

(Received 20 November 2025; revised 30 July 2026; accepted 20 October 2026; published 12 November 2026)

Enhancing the many-body gap of a fractional state is crucial for realizing robust fractional excitations. For fractional Chern insulators, existing studies suggest that making flat Chern bands closely resemble the lowest Landau level (LLL) seems to maximize the excitation gap, providing an apparently optimal platform. In this work, we demonstrate that *deforming away* from the LLL limit can, in fact, produce substantially larger fractional quantum Hall gaps. Using moiré flat bands with strongly non-Landau-level wave functions, we show that the gap can exceed that of the LLL by more than two orders of magnitude for short-range interactions and by factors of two to three for long-range interactions. This enhancement is generic across Abelian fractional Chern insulator states and follows a universal enhancement factor within each hierarchy. In the Landau-level framework, we identify the amplification of pseudopotentials as the microscopic origin of the observed enhancement. More generally, in a Chern band system where the pseudopotential decomposition is not well defined, we find a sharp scaling distinction: in the strongly screened regime, the $\nu = 1/3$ gap scales cubically with gate distance d_s in the LLL and vortexable Chern bands, but linearly in higher-vortexable Chern bands. The activation of this leading $O(d_s)$ term by deviating from ideal quantum geometry is the key origin of the gap enhancement, and this criterion remains meaningful even without rotational symmetry. We further examined non-Abelian states and found that within finite-size resolution, this wave-function construction method can also be used to manipulate and enhance the gap for certain interaction parameters. We further discuss experimental implications of our findings in twisted bilayer $MoTe_2$.

DOI: 10.1103/5yrq-qjkh

I. INTRODUCTION

In the study of fractional quantum Hall (FQH) states [1,2] and fractional Chern insulators (FCIs) [3–31], a key open question is how to enhance the many-body gap[1] of fractional states so that their exotic properties remain robust at higher temperatures and resilient against disorder. For FCIs, a common guiding principle in the literature has been Landau-level mimicry: using a flat Chern band whose properties mimic those of the lowest Landau level (LLL). Model studies show that adiabatically deforming a flat Chern band toward the LLL—by making its Berry curvature more uniform and approaching the ideal geometric condition—can enhance the excitation gap [10–13,15,18,21,22,28]. Likewise, for non-Abelian fractional states, numerical studies indicate that the first Landau level provides a more favorable environment than known moiré flat bands [32]. The mimicry paradigm can be summed up in the following hypothesis: while flat Chern bands can emulate Landau levels, for the same interaction strength, they typically exhibit smaller excitation gaps than the LLL for Abelian fractional states.

In this paper, we demonstrate the opposite. Using moiré flat bands whose wave functions deviate substantially from the Landau level (LL) form, we show that deliberately deforming a Chern band away from the ideal quantum geometry and the LLL limit using higher vortexability can produce significantly larger FQH gaps. For short-range interactions, the fractional gap can exceed the LLL value by as much as two orders of magnitude, whereas for long-range interactions, the enhancement is typically a factor of two to three. To our knowledge, such a systematic enhancement has not been reported in the FCI/FQH literature. Furthermore, this enhancement is generic

[*]These authors contributed equally to this work.
[†]Contact author: danielericparker@ucsd.edu
[‡]Contact author: szl@lanl.gov
[§]Contact author: sunkai@umich.edu

[1]To be clear, by many-body gap, we mean the charge-neutral gap.

Published by the American Physical Society under the terms of the Creative Commons Attribution 4.0 International license. Further distribution of this work must maintain attribution to the author(s) and the published article's title, journal citation, and DOI. Open access publication funded by Max Planck Society.

across Abelian FCI states and, within each hierarchy, follows a universal enhancement factor.

We first demonstrate this effect using a moiré model of a two-dimensional material with a quadratic band touching subjected to a periodic strain potential. Although illustrated in this specific setting, the underlying principles are general and apply broadly to other moiré systems. Within this platform, we construct exact flat Chern bands that resemble both the LLL (with ideal quantum geometry) and higher Landau levels, employing the theoretical framework of higher vortexability [33,34]. By continuously interpolating between these two regimes, we find that the FCI gap reaches its maximum away from the limit of ideal quantum geometry. At fixed interaction strength, the maximal FCI gap surpasses not only the FQH gap of the LLL, but also the gap in flat bands formed from interpolating Landau-level wave functions.

To identify the underlying mechanism, we turn to the Landau-level framework. It is worth noting that in LL systems, extensive effort has been devoted to studying how single-particle wave functions shape the pseudopotentials and thus the many-body gaps—a strategy known as pseudopotential engineering [35–43]. The gap enhancement here stems from the same principle: our construction amplifies the pseudopotentials that set the energy scale of the fractional states. Because flat Chern bands offer a much larger design space, they enable even greater gap enhancement beyond LLs. However, relative angular momentum is generally not conserved in a moiré Chern band since these systems generally do not possess continuous rotation symmetry. Hence a pseudopotential decomposition akin to the LL case is not applicable in these systems. To better understand the origin of this enhancement, we examine the small-d_s scaling of the $\nu = 1/3$ gap across several models. For LL0 and the LLL-like vortexable moiré model, $\Delta_{1/3} \propto d_s^3$, so the gap is rapidly suppressed as $d_s \to 0$. In contrast, LL01 and higher-vortexability moiré bands exhibit $\Delta_{1/3} \propto d_s$ and their gaps decrease much more slowly. This distinction persists in the presence of finite Berry-curvature fluctuations and extends to real material models: chiral twisted bilayer graphene (TBG) follows the cubic law, whereas twisted $MoTe_2$ exhibits linear scaling. The resulting gate-distance dependence provides a direct experimental signature of higher vortexability.

We have also examined non-Abelian (Moore-Read) states and find that for certain interaction parameters, their excitation gap can likewise be enhanced by hybridized wave functions.

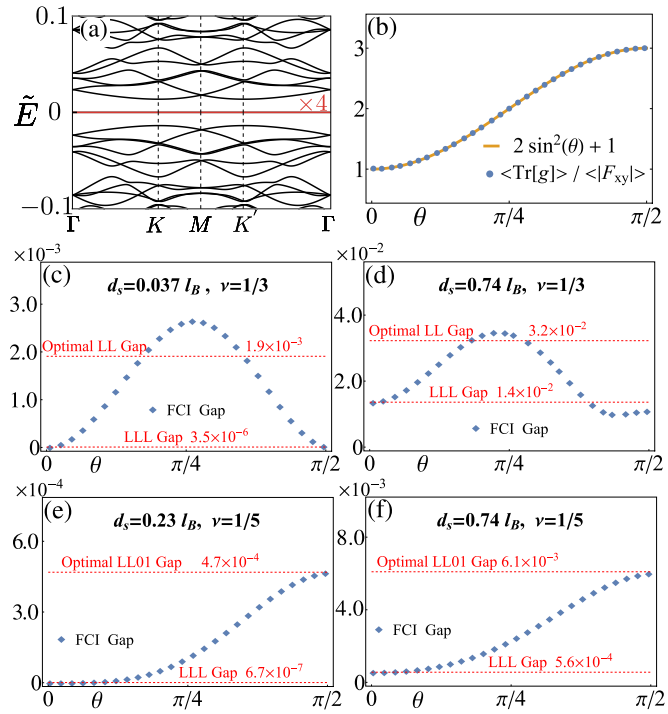


FIG. 1. Many-body gap enhancement in moiré model. (a) Single-particle band structure of the moiré Hamiltonian given by Eq. (1) with fourfold degenerate exact flat bands. The vertical axis in (a) is normalized energy $\tilde{E} = E/(4\pi/\sqrt{3}a)^2$. (b) The ratio between the average trace of the quantum metric $\langle \mathrm{Tr}[g(\mathbf{k})] \rangle$ and the Berry curvature $\langle |F_{xy}(\mathbf{k})| \rangle$ for the higher vortexable band $\tilde{\Psi}_{\mathbf{k},2}$ given in the main text. (c)–(f) Many-body gap of FCI states (blue dots) as a function of θ. The gap increases markedly as θ deviates from the limit of ideal quantum geometry ($\theta = 0$). The lower and upper horizontal red dashed lines in (c)–(f) mark, respectively, the gap of the corresponding FQH states in the LLL and the maximal many-body gap achieved in the LL-hybridization model with the same interaction strength. Notably, in all cases, the moiré model produces a gap that is larger than the LLL gap, and even exceeds the best LL-hybridization model values for $\nu = 1/3$. The gap size here is measured in units of the Coulomb scale, $U_{\mathrm{int}}^{\mathrm{LL}} = e^2/\varepsilon l_B$, where $l_B = 3^{1/4}a/(4\pi)^{1/2}$ is the magnetic length, a is the moiré lattice constant, and ε is the dielectric constant. The parameters used in the exact diagonalization (ED) are (c) $\nu = 1/3$, $d_s/l_B = 0.037$, $N_s = 21$; (d) $\nu = 1/3$, $d_s/l_B = 0.74$, $N_s = 21$; (e) $\nu = 1/5$, $d_s/l_B = 0.23$, $N_s = 25$; and (f) $\nu = 1/5$, $d_s/l_B = 0.74$, $N_s = 25$.

II. MOIRÉ SYSTEM

We consider the following moiré continuum Hamiltonian with chiral symmetry:

$$\mathcal{H}(\mathbf{r}) = \begin{pmatrix} 0 & \mathcal{D}^\dagger(\mathbf{r}) \\ \mathcal{D}(\mathbf{r}) & 0 \end{pmatrix},$$

$$\mathcal{D}(\mathbf{r}) = \begin{pmatrix} -4\overline{\partial}_z^2 + \tilde{A}(\mathbf{r}) & 2i\gamma\overline{\partial}_z \\ 0 & -4\overline{\partial}_z^2 + \tilde{A}(\mathbf{r}) \end{pmatrix}, \qquad (1)$$

where $z = x + iy$ is the complex coordinate, overline denotes complex conjugation, and $\tilde{A}(\mathbf{r}) = A_x(\mathbf{r}) + iA_y(\mathbf{r})$ with $A_x = u_{xx} - u_{yy}$ and $A_y = u_{xy}$ representing moiré-periodic shear strain fields whose form is $\tilde{A}(\mathbf{r}) = -\frac{\alpha}{2}\sum_{n=1}^{3}\{\frac{\eta}{2}e^{i(1-n)\phi}\cos(2\mathbf{G}_n\cdot\mathbf{r}) - \beta e^{i(2-n)\phi}\cos[(\mathbf{G}_n - \mathbf{G}_{n+1})\cdot\mathbf{r}] + e^{i(1-n)\phi}\cos(\mathbf{G}_n\cdot\mathbf{r})\}$, where $\phi = 2\pi/3$, $\mathbf{G}_1 = G(0,1)$, and $\mathbf{G}_{2,3} = G(\mp\sqrt{3}/2, -1/2)$ are the reciprocal lattice vectors, and $G = \frac{4\pi}{\sqrt{3}a}$ with moiré lattice constant a. This Hamiltonian describes a homobilayer system, where the diagonal terms of $\mathcal{D}$ and $\mathcal{D}^\dagger$ represent the intralayer coupling, and the off-diagonal term encodes a momentum-dependent tunneling between the two layers with tunneling amplitude γ. Within each layer, the system hosts a chiral symmetric quadratic band touching (∂_z^2 and $\overline{\partial}_z^2$), and both layers are subjected to the same periodic moiré strain potential $\tilde{A}(\mathbf{r})$ [44,45]. As shown in Fig. 1(a), for $(\alpha, \beta, \eta, \gamma) \approx (4.38G^2, 0.5, -0.9, 100G)$, the moiré field has

a *p6mm* space group symmetry, and the system hosts four exactly flat bands: two polarized on one sublattice with total Chern number $C = +2$ and the other two polarized on the opposite sublattice with $C = -2$. In the following, we focus on the two flat bands with $C = +2$.

As we show analytically in the Supplemental Material (SM [46]; see also Refs. [47–55] therein), one of the two flat-band wave functions takes the form $\Psi_{\mathbf{k},1}(\mathbf{r}) = \{\psi_{\mathbf{k}}^{\mathrm{LLL}}(\mathbf{r}), 0, 0, 0\}h(\mathbf{r})$, where $\psi_{\mathbf{k}}^{\mathrm{LLL}}(\mathbf{r})$ denotes the LLL wave function on a torus and $h(\mathbf{r})$ is a $\mathbf{k}$-independent scalar function such that $|h(\mathbf{r})|$ is moiré periodic [15,22]. Because the $\mathbf{k}$ dependence of this band resides entirely in the $\psi_{\mathbf{k}}^{\mathrm{LLL}}$ term, this flat band shares the same Chern number $C = 1$ and ideal quantum geometry, $\mathrm{Tr}[g(\mathbf{k})] = F_{xy}(\mathbf{k})$, as the LLL. Here, $g(\mathbf{k})$ denotes the quantum metric and $F_{xy}(\mathbf{k})$ the Berry curvature. The second flat-band wave function can be written as $\Psi_{\mathbf{k},2}(\mathbf{r}) = \{l_B\psi_{\mathbf{k}}^{\mathrm{LL1}}(\mathbf{r})/\sqrt{8}, \gamma^{-1}\psi_{\mathbf{k}}^{\mathrm{LLL}}(\mathbf{r}), 0, 0\}h(\mathbf{r})$, where $\psi_{\mathbf{k}}^{\mathrm{LL1}}$ is the wave function of the first LL ($n = 1$) on a torus and $l_B = 3^{1/4}a/(4\pi)^{1/2}$ is the magnetic length corresponding to one magnetic flux quantum per moiré unit cell. As γ varies from 0 to ∞, the wave function $\Psi_{\mathbf{k},2}$ continuously interpolates between a generalized LLL wave function and a generalized first-LL wave function. For convenience, we define $\tan\theta \equiv l_B\gamma/\sqrt{8}$ such that $\theta = 0$ and $\pi/2$ correspond to $\gamma = 0$ and ∞, respectively; in this parametrization, $\Psi_{\mathbf{k},2}(\mathbf{r}) = \{\sin\theta\psi_{\mathbf{k}}^{\mathrm{LL1}}(\mathbf{r}), \cos\theta\psi_{\mathbf{k}}^{\mathrm{LLL}}(\mathbf{r}), 0, 0\}h(\mathbf{r})$. We note that the model's precise strain profile and tuning path are not essential; the same physics should arise in any Chern-band model with analogous projected form factors.

If $h(\mathbf{r}) = 1$, the wave functions above reduce to LL wave functions, and both the Berry curvature $F_{xy}(\mathbf{k})$ and the trace of the quantum metric $\mathrm{Tr}[g(\mathbf{k})]$ remain perfectly homogeneous in momentum space. For flat Chern bands, in contrast, the absence of net magnetic flux, together with the Bloch theorem, requires $h(\mathbf{r})$ to be spatially inhomogeneous. As shown in the SM [46], our model exhibits a strongly inhomogeneous $h(\mathbf{r})$, causing the wave functions $\Psi_{\mathbf{k},1}$ and $\Psi_{\mathbf{k},2}$ to deviate substantially from those of Landau-level systems. Typically, such inhomogeneity in $h(\mathbf{r})$ would induce pronounced variations in the Berry curvature $F_{xy}(\mathbf{k})$ and the trace of the quantum metric $\mathrm{Tr}[g(\mathbf{k})]$ across momentum space [15,22,56,57]. Here, however, we choose the moiré potential so that despite the spatial modulation of $h(\mathbf{r})$, both $F_{xy}(\mathbf{k})$ and $\mathrm{Tr}[g(\mathbf{k})]$ remain nearly homogeneous, with $\mathbf{k}$-space fluctuations below 5% (see the SM [46]). This near uniformity provides a clean setting and can improve the absolute gap [56], but it is neither necessary nor sufficient for the enhancement observed here. Related gap-enhancement results along Jain sequences are shown in Fig. 2. We show examples with nonuniform geometry later in Fig. 3 and Appendix C.

Due to the inhomogeneity of $h(\mathbf{r})$, the states $\Psi_{\mathbf{k},1}$ and $\Psi_{\mathbf{k},2}$ are not orthogonal. We therefore define the orthogonalized wave functions as $\tilde{\Psi}_{\mathbf{k},1} = \Psi_{\mathbf{k},1}$ and $\tilde{\Psi}_{\mathbf{k},2} = \Psi_{\mathbf{k},2} - \langle\Psi_{\mathbf{k},1}|\Psi_{\mathbf{k},2}\rangle\Psi_{\mathbf{k},1}/||\Psi_{\mathbf{k},1}||^2$. Physically, these are the bands that are expected to be fully filled and fully empty at filling $\nu = 1$ in the presence of quasi-long-range interactions. As the parameter θ is varied, $\tilde{\Psi}_{\mathbf{k},2}$ retains Chern number $C = 1$, while the ratio $\langle\mathrm{Tr}[g(\mathbf{k})]\rangle/\langle F_{xy}(\mathbf{k})\rangle = 1 + 2\sin^2\theta$, as was shown in [34], evolving from $\lim_{\theta\to 0}\mathrm{Tr}[g(\mathbf{k})]/F_{xy}(\mathbf{k}) = 1$ to $\lim_{\theta\to\pi/2}\langle\mathrm{Tr}[g(\mathbf{k})]\rangle/\langle F_{xy}(\mathbf{k})\rangle = 3$, as shown in Fig. 1(b). At

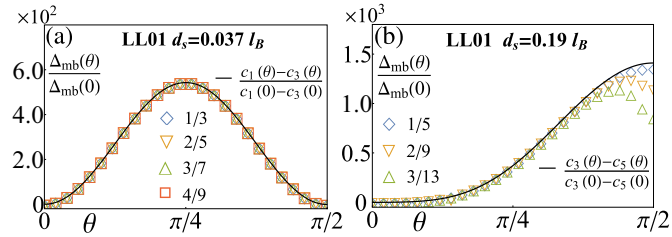


FIG. 2. Universal gap enhancement along Jain sequences. Normalized many-body gap $\Delta_{\mathrm{mb}}(\theta)/\Delta_{\mathrm{mb}}(0)$ for the LL01 hybridization model. (a) 1/3 *sequence:* $\nu = 1/3$, 2/5, 3/7, 4/9 at short-distance screening $d_s/l_B = 0.037$. The enhancement exhibits a universal domelike profile across the entire sequence, following the pseudopotential c_1–c_3 and peaking near $\theta = \pi/4$. (b) 1/5 *sequence:* $\nu = 1/5$, 2/9, 3/13 at $d_s/l_B = 0.19$. Here, the θ dependence tracks the pseudopotential c_3–c_5 throughout the sequence, with the maximum occurring near $\theta = \pi/2$.

$\theta = 0$, this band satisfies the ideal quantum geometry condition $\mathrm{Tr}[g(\mathbf{k})]/F_{xy}(\mathbf{k}) = 1$, and thus belongs to the family of "vortexable" flat bands [28], for which Laughlin-type wave functions can be constructed at fractional fillings, forming exact zero modes of the Haldane pseudopotentials [15,22]. On the other hand, for $\theta > 0$, where $\langle\mathrm{Tr}[g(\mathbf{k})]\rangle/\langle F_{xy}(\mathbf{k})\rangle > 1$, it belongs to the family of "first (higher) vortexable" bands [33,34], where non-Abelian FCI states have been predicted.

We focus on the flat band spanned by $\tilde{\Psi}_{\mathbf{k},2}$. To study the FCIs that it can host, we consider projected repulsive interactions,

$$H_{\mathrm{int}} = \frac{1}{2A}\sum_{\mathbf{q}} V(\mathbf{q}) \,:\, \rho(\mathbf{q})\,\rho(-\mathbf{q}) \,:, \tag{2}$$

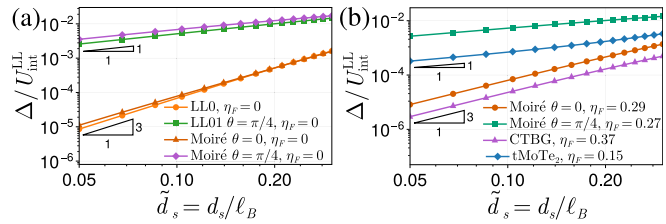


FIG. 3. Distinct short-range screening gap scaling laws at $\nu = 1/3$. The neutral gap $\Delta/U_{\mathrm{int}}^{\mathrm{LL}}$ is plotted on log-log axes against $\tilde{d}_s = d_s/l_B$, $U_{\mathrm{int}}^{\mathrm{LL}} = e^2/\varepsilon l_B$; black triangles indicate (relative) slopes 1 and 3, corresponding to the gap linear scaling and cubic scaling with d_s. (a) For models with vanishing Berry-curvature fluctuation $\eta_F \equiv \mathrm{Std}(|F_{xy}|)/\langle|F_{xy}|\rangle$, LL0 and the vortexable moiré band at $\theta = 0$ follow the cubic law, whereas LL01 and the higher-vortexable moiré band at $\theta = \pi/4$ follow the linear law. (b) The same distinction persists for nonuniform Berry curvature: the moiré band at $\theta = 0$ and chiral twisted bilayer graphene (CTBG) are cubic, while the higher-vortexable moiré band at $\theta = \pi/4$ and the continuum twisted $MoTe_2$ are approximately linear. The moiré Hamiltonian used for (a) is the same as that in Fig. 1 and the moiré model used in (b) is the same as in Eq. (1) with $\tilde{A}(\mathbf{r}) = -\frac{\alpha}{2}\sum_{n=1}^{3} e^{i(1-n)\phi}\cos(\mathbf{G}_n\cdot\mathbf{r})$, where $\mathbf{G}_n$ and ϕ were defined below Eq. (1), and $\alpha = 0.62|G|^2$. For twisted $MoTe_2$, we use a twist angle of 3.7° and dielectric constant $\varepsilon = 5$ [66–68]. The single-particle dispersion of twisted $MoTe_2$ is set to zero to isolate the effect of the projected interaction.

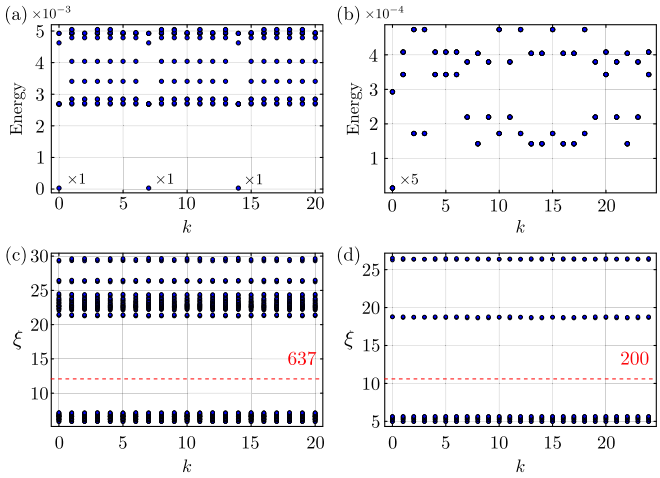


FIG. 4. (a), (b) Many-body energy spectra at filling $\nu = 1/3$, $d_s/l_B = 0.037$ and $\nu = 1/5$, $d_s/l_B = 0.23$, respectively. The energy is normalized by $U_{\rm int}^{\rm LL}$ as in Fig. 1. (c), (d) Particle entanglement spectra of the ground states in (a), (b) with particle cuts $N_A = 3, N_B = 4$ for $\nu = 1/3$ and $N_A = 2, N_B = 3$ for $\nu = 1/5$, respectively. The number of low-lying states below the red dashed lines (as written in red) matches the quasihole counting of Laughlin states at the respective filling fractions [7]. $\theta = \pi/4$ was used for all cases.

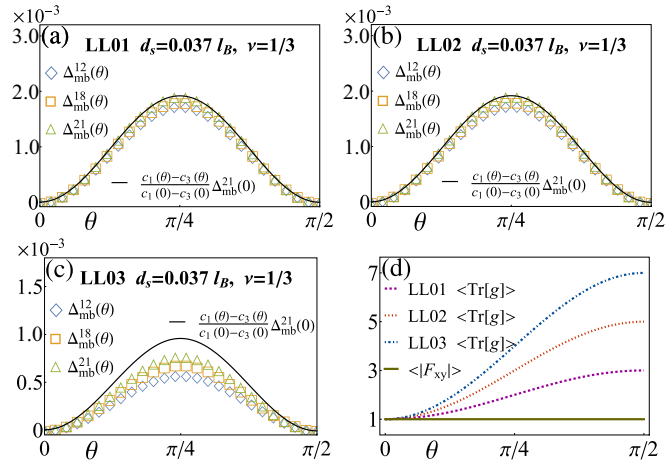


FIG. 5. Gap enhancement via Landau-level hybridization and pseudopotential decomposition. (a)–(c) Many-body gap and pseudopotentials as functions of the hybridization parameter θ, for LL01, LL02, and LL03, respectively. As in Fig. 1, the energy is measured in units of the Coulomb energy scale $U_{\rm int}^{\rm LL}$. Panel (d) shows the average trace of quantum metric and Berry curvature normalized by l_B^2 for the three models. Gap values are obtained for multiple finite clusters (see SM [46]), using screened Coulomb interactions with screening length $d_s = 0.037\, l_B$. The gap reaches its maximum near $\theta \approx \pi/4$, showing up to ∼500-fold enhancement for LL01 and LL02, with peak gap values of ∼0.2% of the Coulomb scale (compared to 0.0003% for the LLL). For LL03, the enhancement is smaller–about ∼200-fold, yielding a maximum gap ∼0.06% of the Coulomb scale.

where A is the system area, colons denote normal ordering, and $V(\mathbf{q}) = 2\pi e^2 \tanh(d_s q)/(\varepsilon q)$ is the screened Coulomb interaction. Here, d_s is the distance from the electron plane to either of the two symmetric screening gates. The projected density operator is $\rho(\mathbf{q}) = \sum_{\mathbf{k}} \lambda_{\mathbf{q}}(\mathbf{k}) c_{\mathbf{k}}^\dagger c_{\mathbf{k}+\mathbf{q}}$, with form factor $\lambda_{\mathbf{q}}(\mathbf{k}) = \langle \tilde{\Psi}_{\mathbf{k},2}(\mathbf{r}) | e^{-i\mathbf{q}\cdot\mathbf{r}} | \tilde{\Psi}_{\mathbf{k}+\mathbf{q},2}(\mathbf{r}) \rangle$. We perform numerical exact diagonalization at filling fractions $\nu = 1/3$ and $\nu = 1/5$ for θ values between 0 and $\pi/2$. At both fillings, and for the entire range of θ, the ground state is found to be an FCI with many-body Chern number $C_{\rm mb} = \nu$ (see Appendix A and Fig. 4 for the many-body spectra and particle entanglement spectra at a representative angle $\theta = \pi/4$). To quantify the stability of the FCI, Figs. 1(c)–1(f) show the many-body excitation gap $\Delta_{\rm mb}$ as a function of θ for different screening lengths d_s. Remarkably, the FCI gap is enhanced dramatically as θ increases, which tunes the band *away* from ideal quantum geometry. For comparison, Figs. 1(c)–1(f) also show the excitation gap for FQH states with the same interaction parameters in the LLL (lower dashed horizontal lines) and the maximum gap obtainable from the LL-hybridization model introduced later in the text (upper dashed horizontal lines; see Fig. 5). The gap of the present moiré model can exceed both benchmarks for suitable values of θ.

For $\nu = 1/3$ with short-range screening $d_s/l_B = 0.037$ [Fig. 1(c)], the gap develops a maximum near $\theta = \pi/4$, reaching values of more than two orders of magnitude above the LLL baseline. By contrast, with longer-range interactions $d_s/l_B = 0.74$ [Fig. 1(d)], the enhancement is far milder. There the gap increases by about a factor of two, before decreasing. For $\nu = 1/5$, the largest gaps appear when the model approaches the generalized first Landau level ($\theta = \pi/2$), and again the effect is far more pronounced for short screening [$d_s/l_B = 0.23$, Fig. 1(e)] than for long-range interactions [$d_s/l_B = 0.74$, Fig. 1(f)].

In Fig. 6, we show a many-body gap for another moiré model with much larger quantum geometric fluctuations. Remarkably, the qualitative features of gap enhancement remain the same, even away from uniform quantum geometric distribution, although the overall gap sizes reduce in comparison with the model in Fig. 1, suggesting that many-body gap enhancement as a function of θ may be universal.

III. LL-HYBRIDIZATION MODEL

To understand the mechanism responsible for the many-body gap enhancement away from the vortexable limit, we construct a simplified "toy model" Hamiltonian that hybridizes two chosen Landau levels (LLs) labeled by n_1 and n_2. This type of mixed LL wave function has been studied before in [41–43,58]. Denoting the corresponding single-particle wave functions as $|\psi^{{\rm LL}n_1}\rangle$ and $|\psi^{{\rm LL}n_2}\rangle$, we define a two-component spinor wave function,

$$\Psi_{n_1,n_2}(\theta) = \begin{pmatrix} \sin\theta\, |\psi^{{\rm LL}n_2}\rangle \\ \cos\theta\, |\psi^{{\rm LL}n_1}\rangle \end{pmatrix}, \qquad \theta \in [0, \pi/2], \tag{3}$$

where the hybridization parameter θ continuously interpolates between the two LLs. Below, we will use LLn_1n_2 to label these models. For LL01, $\Psi_{0,1}(\theta)$ coincides with $\Psi_{\mathbf{k},2}$ introduced early on, if $h(\mathbf{r})$ is set to unity. We can further introduce the following Hamiltonian:

$$\mathcal{H}_{n_2-n_1}(m) = \begin{pmatrix} m & (a^\dagger)^{n_2-n_1} \\ (a)^{n_2-n_1} & -m \end{pmatrix}, \tag{4}$$

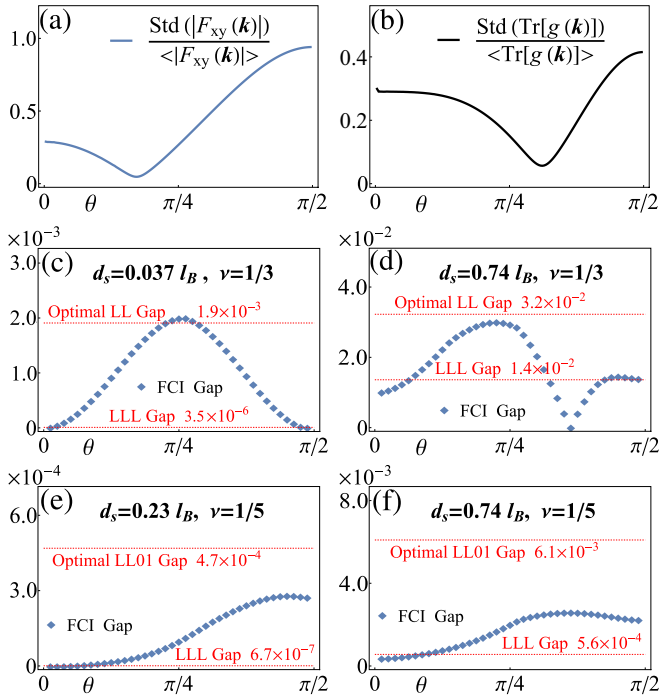


FIG. 6. Many-body gap enhancement in a moiré model with significant single-particle quantum geometric fluctuations. The single-particle Hamiltonian is the same as in Eq. (1) with $\tilde{A}(\mathbf{r}) = -\alpha \sum_{n=1}^{3} e^{i(1-n)\phi} \cos(\mathbf{G}_n \cdot \mathbf{r})/2$, where $\mathbf{G}_n$ and ϕ were defined below Eq. (1), and $\alpha = 0.62|G|^2$. Similar to Fig. 1(a), there are four exact flatbands, two per sublattice. One of these two sublattice polarized bands is vortexable with wave function $\tilde{\Psi}_{\mathbf{k},1}(\mathbf{r})$, the other one is higher vortexable $\tilde{\Psi}_{\mathbf{k},2}(\mathbf{r})$ as discussed in the main text. (a), (b) The fluctuations of Berry curvature and quantum metric for the higher-vortexable band $\tilde{\Psi}_{\mathbf{k},2}(\mathbf{r})$, respectively. Clearly, for this choice of $\tilde{A}(\mathbf{r})$, the fluctuations in Berry curvature and quantum metric are much larger than those in Fig. 1. (c)–(f) Many-body gap of FCI states (blue dots) from ED as a function of θ. As in Fig. 1, the energy is measured in units of the Coulomb energy scale $U_{\text{int}}^{\text{LL}}$. The parameters used in ED for (c)–(f) are the same as those used in Figs. 1(c)–1(f), respectively. The lower and upper horizontal red dashed lines in (c)–(f) mark, respectively, the gap of the corresponding FQH states in the LLL and the maximal many-body gap achieved in the LL-hybridization model with the same interaction strength. Gap-enhancement trends in this case remain the same as in Fig. 1, although the maximum gap enhancements are significantly lower than those in Fig. 1; the gap sizes do not follow the variation in tr(g) and F_{xy}. In (d), a phase transition occurs at $\theta \approx 1.18$; our analysis here focuses on the maximum gap of the FCI phase.

where a and $a^\dagger$ are Landau-level lowering and raising operators, respectively, and m is a mass parameter. Without loss of generality, we take $n_2 > n_1$. With the identification $\tan\theta = (\sqrt{E(n_1,n_2)^2 + m^2} + m)/E(n_1,n_2)$, where $E(n_1,n_2) = \sqrt{n_2!/n_1!}$, one can verify that $\Psi_{n_1,n_2}(\theta)$ is an eigenstate of $\mathcal{H}_{n_2-n_1}(m)$ with eigenvalue $\sqrt{E(n_1,n_2)^2 + m^2}$. The relation between θ and m implies that $\theta = 0, \pi/4$, and $\pi/2$ correspond to $m = -\infty, 0$, and ∞. Notably, this Hamiltonian is the effective Hamiltonian of multilayer rhombohedral graphene with $n_2 - n_1 > 1$ layers, subject to an out-of-plane magnetic field and a displacement field that controls the mass parameter m [59]. The special case $\mathcal{H}_1(m)$ describes graphene LLs in a magnetic field with a C_{2z} breaking term m; this mass m disappears at $\theta = \pi/4$, and the wave function $\Psi_{n,n+1}(\pi/4)$ corresponds to the $(n+1)$-th Landau level of graphene [60–62].

This LL-hybridization model exhibits the same gap-enhancement phenomenon as the moiré model. We project the screened Coulomb interaction to the hybridized band in Eq. (3). The resulting $\nu = 1/3$ gap enhancement is summarized in Appendix B, Fig. 5, while Fig. 2 shows that the same gap-enhancement behavior extends across the Jain sequences. To understand this, we turn to pseudopotentials.

IV. HALDANE PSEUDOPOTENTIALS

In a rotationally invariant Landau-level system, the projected two-body interaction can be decomposed into channels of definite relative angular momentum [63–65]. LL hybridization modifies these channels through the cyclotron form factor,

$$F(q;\theta) = \left[\cos^2\theta L_{n_1}\left(\frac{q^2 l_B^2}{2}\right) + \sin^2\theta L_{n_2}\left(\frac{q^2 l_B^2}{2}\right)\right] e^{-\frac{q^2 l_B^2}{4}}, \tag{5}$$

where $L_n(x)$ is the nth Laguerre polynomial. The effective interaction after projection is $V_{\text{eff}}(q;\theta) = V(q)[F(q;\theta)]^2$. Once the effective interaction is specified, the problem can be characterized by the pseudopotential coefficients,

$$c_m(\theta) = \int \frac{d^2\mathbf{q}}{(2\pi)^2} V_{\text{eff}}(q;\theta)\, v_m(q), \qquad m = 0, 1, 2, \ldots, \tag{6}$$

where

$$v_m(q) = e^{-q^2 l_B^2/2} L_m\left(q^2 l_B^2\right) \tag{7}$$

characterizes the momentum-space profile of a two-particle state with relative angular momentum m.

LL hybridization therefore redistributes interaction strength among the pseudopotential channels $\{c_m\}$. This explains the gap-enhancement behavior in Fig. 2. For the $\nu = n/(2n+1)$ sequence, the gap evolution closely follows c_1–c_3. In the short-range limit of the LL01 model, $c_3 \to 0$, $c_1 \propto \sin^2(2\theta)$, producing the common maximum near $\theta = \pi/4$. For the $\nu = n/(4n+1)$ sequence, the relevant channel is instead c_3–c_5, whose maximum shifts toward $\theta = \pi/2$ at finite screening length. The same picture can be generalized to any LL hybridizations. Detailed calculations for LL01, LL02, and LL03 hybridizations are provided in Appendix B. The analytic expressions and finite-screening-length comparisons are provided in the Supplemental Material [46].

V. SHORT-SCREENING SCALING

The pseudopotential analysis above is only applicable in Landau-level models which possess continuous rotation symmetry. To identify a more general mechanism for gap enhancement that remains meaningful in higher vortexable bands without continuous rotation symmetry, we examine the strongly screened limit of small d_s. The discussion below is for 1/3 filling states, but it can be extended to other Jain

sequence states. In this limit, the interaction can be expanded as $V(q) = \frac{2\pi e^2}{\varepsilon q}\tanh(qd_s) = \frac{2\pi e^2}{\varepsilon}[d_s - q^2 d_s^3/3 + O(d_s^5)]$. The first term in this expansion describes contact interaction, and hence it vanishes for electrons in the LLL with single-component wave functions due to fermion antisymmetry. The first nonzero contribution is therefore $O(q^2 d_s^3)$, giving $\Delta_{1/3}^{\mathrm{LLL}} \propto d_s^3$. In a multicomponent higher-vortexable Chern band ($0 < \theta < \pi/2$), the matrix elements of the contact interaction can remain nonzero, so the leading gap can instead obey $\Delta_{1/3}^{\mathrm{FCI}} \propto d_s$. Figure 3(a) confirms these two scaling laws across the LL-hybridization models (in Fig. 2) and moiré models (in Fig. 1) considered above. More importantly, we tested these scalings on experimentally relevant systems such as twisted-$MoTe_2$ and TBG. In particular, twisted-$MoTe_2$ is multicomponent and exhibits nonideal quantum geometry, and its many-body gap scales linearly with d_s. This behavior suggests that it may belong to the family of multicomponent higher-vortexable bands. By contrast, the chiral TBG calculation exhibits cubic scaling, $\Delta_{1/3} \propto d_s^3$, which agrees with the expectation for a vortexable band with ideal quantum geometry, despite its multicomponent nature. These examples confirm that the nonzero contribution of the contact potential is at the heart of the gap enhancement, and is independent of exact continuous rotational symmetry or uniform quantum geometry. In the SM [46], we further prove that for (i) single or multicomponent vortexable bands and (ii) single-component higher-vortexable bands, the many-body gap at 1/3 filling must scale as d_s^3; and hence a multicomponent higher-vortexable band is essential for the many-body gap to scale as d_s. Because d_s is set by the distance to screening gates, the different scaling law provides a direct experimental signature: upon reducing the gate distance, a higher-vortexable band with an active projected local interaction loses its gap much more slowly than an LLL-like band. Similarly, for ideal bands at filling $\nu = 1/5$, the many-body gap generically scales as $\Delta \propto d_s^7$, whereas in higher-vortexable bands, the leading scaling can be reduced to $\Delta \propto d_s^3$ or $\Delta \propto d_s$. This distinction underlies the substantial gap enhancement observed at $\nu = 1/5$.

VI. NON-ABELIAN STATES

This hybridization-based approach can also enhance the excitation gap of non-Abelian states [41–43]. As shown in Fig. 7, using screened Coulomb interactions with a short screening length $d_s/l_B = 0.5$, the energy gap of the Moore-Read state increases as we switch from the $n = 1$ LL to hybridized wave functions composed of the lowest three LLs. Owing to their intrinsic complexity and stronger finite-size effects, non-Abelian states are considerably more intricate than their Abelian counterparts. Consequently, further studies will be needed to fully elucidate the connection between the excitation gap and the hybridized wave functions.

VII. DISCUSSION

In addition to the hybridization between two LLs, in the SM [46] we also consider mixing among multiple Landau levels. Among all the cases studied, for filling factor $\nu = 1/3$, we find that the largest many-body gap occurs for the LL01 hybridization with $\theta = \pi/4$ in the presence of short-range interactions, and at $\theta = 0.2\pi$ for long-range

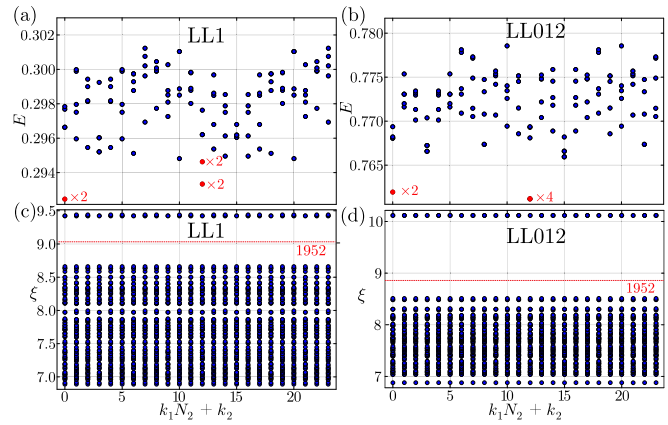


FIG. 7. (a), (b) Many-body energy spectra at filling $\nu = 1/2$ and $d_s/l_B = 0.5$. Here we consider a triangular lattice of size $N_1 \times N_2 = 4 \times 6$. The red dots indicate Moore-Read states exhibiting sixfold quasidegeneracy. (a) In the $n = 1$ LL, the Moore-Read state does not display a clear gap. In (b), we use a three-component hybridized wave function constructed from the lowest three Landau levels, $\Psi = (\sqrt{w_0}\psi^{\mathrm{LL0}}, \sqrt{w_1}\psi^{\mathrm{LL1}}, \sqrt{w_2}\psi^{\mathrm{LL2}})$, with $(w_0, w_1, w_2) = (0.273, 0.273, 0.454)$. The gap size here is significantly increased to $0.004\, U_{\mathrm{int}}^{\mathrm{LL}}$. (c), (d) Particle entanglement spectra of the ground states in (a), (b) with particle cut $N_A = 3$, $N_B = 9$. The number of low-lying states below the red dashed lines matches the quasihole counting of the Moore-Read state [7,9].

Coulomb interactions. Since the enhancement of the many-body gap is for LL01 and near $\theta = \pi/4$, it may be seen in the $n = 1$ LL of graphene. For long-range interactions, the pseudopotential enhancement observed here agrees with earlier studies of Dirac-fermion Landau levels reported in Refs. [58,62].

For the moiré model, although the wave functions deviate substantially from LLs due to the highly inhomogeneous function $h(\mathbf{r})$, we find that the hybridization between the generalized lowest and first LL exhibits the same trend of gap enhancement. Moreover, the inhomogeneous form of $h(\mathbf{r})$ appears to further enhance the many-body gap beyond what can be achieved through LL hybridization. The microscopic origin of this additional enhancement remains an interesting question for future study.

For comparison, we present in the SM [46], Sec. VI, a single-component LL-hybridization model (that was previously used in Ref. [34]) that shares identical Berry curvature $F_{xy}(\mathbf{k})$ and quantum metric trace $\mathrm{Tr}[g(\mathbf{k})]$ with the LL-hybridization models discussed above. However, unlike those models—which exhibit a many-body gap enhanced beyond that of the LLL—the comparison model shows a reduced gap smaller than the LLL. This contrast demonstrates that the single-particle quantities $F_{xy}(\mathbf{k})$ and $\mathrm{Tr}[g(\mathbf{k})]$ cannot fully determine the many-body gap.

We also note that in engineered platforms such as photonics, cold atoms, and polaritons, the predominance of short-range interactions has long posed a major obstacle by yielding very small fractional gaps in conventional Landau-level settings. Our results point to a way around this limitation: by exploiting the design principles identified here, short-range interactions can support many-body gaps

enhanced by orders of magnitude. In gated electronic moiré systems, the linear-versus-cubic dependence on gate distance provides a direct way to test this mechanism.

In addition to FCIs, our design principle may also offer a platform for time-reversal-invariant fractional topological insulators (FTIs), as it suppresses the s-wave pseudopotential component c_0 [46], a key ingredient for stabilizing FTIs [69].

ACKNOWLEDGMENTS

The authors thank Siddharth Parameswaran for pointing out the LL-hybridization model. This work was supported in part by Air Force Office of Scientific Research MURI Grant No. FA9550-23-1-0334 and the Office of Naval Research MURI Grant No. N00014-20-1-2479, and by the Gordon and Betty Moore Foundation Award No. N031710 (X.W., Y.Z., and K.S.). The work at LANL (S.-Z.L.) was carried out under the auspices of the U.S. DOE NNSA under Contract No. 89233218CNA000001 through the LDRD Program, was supported by the Center for Nonlinear Studies at LANL, and was performed, in part, at the Center for Integrated Nanotechnologies, an Office of Science User Facility operated for the U.S. Department of Energy Office of Science, under user Proposals No. 2018BU0010 and No. 2018BU0083.

DATA AVAILABILITY

There are no publicly available research data or software supporting this manuscript. Requests for further information or data should be sent to the authors.

APPENDIX A: MANY-BODY ENERGY SPECTRA AND PARTICLE ENTANGLEMENT SPECTRA FOR $\nu = 1/3$ AND $\nu = 1/5$ FCI GROUND STATES

Figure 4 presents the many-body energy spectra and particle entanglement spectra for $\nu = 1/3$ and $\nu = 1/5$ FCI ground states.

APPENDIX B: GAP ENHANCEMENT AND PSEUDOPOTENTIALS IN THE LL-HYBRIDIZATION MODEL

For clarity, we collect the LL-hybridization results in this appendix. This construction provides a clean and controlled model for isolating the mechanism of gap enhancement. These results further show that the gap evolution is governed by the projected interaction, rather than by the average quantum metric alone.

This LL-hybridization model exhibits the same gap-enhancement phenomena as the moiré model. Explicitly, we consider the same screened Coulomb interaction, $V(q) = 2\pi e^2 \tanh(qd_s)/(\varepsilon q)$. We project this interaction onto the hybridized band defined in Eq. (3) and perform exact diagonalization on a torus. Figure 5 shows that the $\nu = 1/3$ Laughlin-state gap is strongly enhanced at intermediate values of θ. For LL01 and LL02 hybridizations, the maximum is more than 500 times the LLL gap, with a more modest ∼200-fold enhancement in the LL03 case.

We also computed the pseudopotential coefficients c_m, both analytically and numerically (see the SM [46]). As θ varies, the key term c_1, which stabilizes the $\nu = 1/3$ Laughlin state, exhibits the same θ-dependent trend as the many-body excitation gap. To quantify this, Fig. 5 plots the pseudopotential difference, $c_1(\theta) - c_3(\theta)$, normalized by the $\theta = 0$ values of the many-body gap and pseudopotentials, $\Delta_{\mathrm{mb}}(0)/[c_1(0) - c_3(0)]$. The θ dependence of c_1–c_3 closely tracks the enhancement of the many-body gap.

For LL01 and LL02 in the short-range limit ($d_s \ll l_B$), the pseudopotentials satisfy $c_1 \propto \sin^2(2\theta)$, while $c_3 = c_5 = 0$. The many-body gap follows the same θ dependence, peaking at $\theta = \pi/4$. The model LL03 shows a sizable c_3 contribution, and the reduced difference $c_1 - c_3$ correlates with a more moderate ∼200-fold gap enhancement; see Fig. 5(c). Although the short-range limit provides analytical simplicity, it is not essential; both the pseudopotential and gap enhancements persist for finite screening lengths, as shown in the SM [46]. These results demonstrate that the observed gap enhancement originates from the θ-dependent evolution of the pseudopotentials.

APPENDIX C: MANY-BODY GAP ENHANCEMENT OF ABELIAN STATES IN A MOIRÉ MODEL WITH SIGNIFICANT SINGLE-PARTICLE QUANTUM GEOMETRIC FLUCTUATIONS

Figure 6 displays the many-body gap enhancement of Abelian states in a moiré model with significant single-particle quantum geometric fluctuations.

APPENDIX D: MANY-BODY GAP ENHANCEMENT OF NON-ABELIAN MOORE-READ STATE VIA LL HYBRIDIZATION

Figure 7 shows the many-body gap enhancement of the non-Abelian Moore-Read state via LL hybridization.

[1] H. L. Stormer, D. C. Tsui, and A. C. Gossard, The fractional quantum Hall effect, Rev. Mod. Phys. **71**, S298 (1999).
[2] R. B. Laughlin, Nobel lecture: Fractional quantization, Rev. Mod. Phys. **71**, 863 (1999).
[3] E. Tang, J.-W. Mei, and X.-G. Wen, High-temperature fractional quantum Hall states, Phys. Rev. Lett. **106**, 236802 (2011).
[4] K. Sun, Z. Gu, H. Katsura, and S. Das Sarma, Nearly flatbands with nontrivial topology, Phys. Rev. Lett. **106**, 236803 (2011).
[5] T. Neupert, L. Santos, C. Chamon, and C. Mudry, Fractional quantum Hall states at zero magnetic field, Phys. Rev. Lett. **106**, 236804 (2011).

[6] D. N. Sheng, Z.-C. Gu, K. Sun, and L. Sheng, Fractional quantum Hall effect in the absence of Landau levels, Nat. Commun. **2**, 389 (2011).

[7] N. Regnault and B. A. Bernevig, Fractional Chern insulator, Phys. Rev. X **1**, 021014 (2011).

[8] D. Xiao, W. Zhu, Y. Ran, N. Nagaosa, and S. Okamoto, Interface engineering of quantum Hall effects in digital transition metal oxide heterostructures, Nat. Commun. **2**, 596 (2011).

[9] B. A. Bernevig and N. Regnault, Emergent many-body translational symmetries of Abelian and non-Abelian fractionally filled topological insulators, Phys. Rev. B **85**, 075128 (2012).

[10] Y.-H. Wu, J. K. Jain, and K. Sun, Adiabatic continuity between Hofstadter and Chern insulator states, Phys. Rev. B **86**, 165129 (2012).

[11] S. A. Parameswaran, R. Roy, and S. L. Sondhi, Fractional quantum Hall physics in topological flat bands, C. R. Phys. **14**, 816 (2013).

[12] R. Roy, Band geometry of fractional topological insulators, Phys. Rev. B **90**, 165139 (2014).

[13] Y.-H. Wu, J. K. Jain, and K. Sun, Fractional topological phases in generalized Hofstadter bands with arbitrary Chern numbers, Phys. Rev. B **91**, 041119(R) (2015).

[14] C. Repellin and T. Senthil, Chern bands of twisted bilayer graphene: Fractional Chern insulators and spin phase transition, Phys. Rev. Res. **2**, 023238 (2020).

[15] P. J. Ledwith, G. Tarnopolsky, E. Khalaf, and A. Vishwanath, Fractional Chern insulator states in twisted bilayer graphene: An analytical approach, Phys. Rev. Res. **2**, 023237 (2020).

[16] S. H. Simon and M. S. Rudner, Contrasting lattice geometry dependent versus independent quantities: Ramifications for Berry curvature, energy gaps, and dynamics, Phys. Rev. B **102**, 165148 (2020).

[17] Z. Liu, A. Abouelkomsan, and E. J. Bergholtz, Gate-tunable fractional Chern insulators in twisted double bilayer graphene, Phys. Rev. Lett. **126**, 026801 (2021).

[18] B. Mera and T. Ozawa, Engineering geometrically flat Chern bands with Fubini-Study Kähler structure, Phys. Rev. B **104**, 115160 (2021).

[19] H. Li, U. Kumar, K. Sun, and S.-Z. Lin, Spontaneous fractional Chern insulators in transition metal dichalcogenide moiré superlattices, Phys. Rev. Res. **3**, L032070 (2021).

[20] T. Devakul, V. Crépel, Y. Zhang, and L. Fu, Magic in twisted transition metal dichalcogenide bilayers, Nat. Commun. **12**, 6730 (2021).

[21] P. J. Ledwith, E. Khalaf, and A. Vishwanath, Strong coupling theory of magic-angle graphene: A pedagogical introduction, Ann. Phys. **435**, 168646 (2021).

[22] J. Wang, J. Cano, A. J. Millis, Z. Liu, and B. Yang, Exact Landau level description of geometry and interaction in a flatband, Phys. Rev. Lett. **127**, 246403 (2021).

[23] Y. Xie, A. T. Pierce, J. M. Park, D. E. Parker, E. Khalaf, P. Ledwith, Y. Cao, S. H. Lee, S. Chen, P. R. Forrester, K. Watanabe, T. Taniguchi, A. Vishwanath, P. Jarillo-Herrero, and A. Yacoby, Fractional Chern insulators in magic-angle twisted bilayer graphene, Nature (London) **600**, 439 (2021).

[24] J. Cai, E. Anderson, C. Wang, X. Zhang, X. Liu, W. Holtzmann, Y. Zhang, F. Fan, T. Taniguchi, K. Watanabe, Y. Ran, T. Cao, L. Fu, D. Xiao, W. Yao, and X. Xu, Signatures of fractional quantum anomalous Hall states in twisted $MoTe_2$, Nature (London) **622**, 63 (2023).

[25] Y. Zeng, Z. Xia, K. Kang, J. Zhu, P. Knüppel, C. Vaswani, K. Watanabe, T. Taniguchi, K. F. Mak, and J. Shan, Thermodynamic evidence of fractional Chern insulator in moiré $MoTe_2$, Nature (London) **622**, 69 (2023).

[26] H. Park, J. Cai, E. Anderson, Y. Zhang, J. Zhu, X. Liu, C. Wang, W. Holtzmann, C. Hu, Z. Liu, T. Taniguchi, K. Watanabe, J.-H. Chu, T. Cao, L. Fu, W. Yao, C.-Z. Chang, D. Cobden, D. Xiao, and X. Xu, Observation of fractionally quantized anomalous Hall effect, Nature (London) **622**, 74 (2023).

[27] F. Xu, Z. Sun, T. Jia, C. Liu, C. Xu, C. Li, Y. Gu, K. Watanabe, T. Taniguchi, B. Tong, J. Jia, Z. Shi, S. Jiang, Y. Zhang, X. Liu, and T. Li, Observation of integer and fractional quantum anomalous Hall effects in twisted bilayer $MoTe_2$, Phys. Rev. X **13**, 031037 (2023).

[28] P. J. Ledwith, A. Vishwanath, and D. E. Parker, Vortexability: A unifying criterion for ideal fractional Chern insulators, Phys. Rev. B **108**, 205144 (2023).

[29] A.-K. Wu, S. Sarkar, X. Wan, K. Sun, and S.-Z. Lin, Quantum-metric-induced quantum Hall conductance inversion and reentrant transition in fractional Chern insulators, Phys. Rev. Res. **6**, L032063 (2024).

[30] Z. Lu, T. Han, Y. Yao, A. P. Reddy, J. Yang, J. Seo, K. Watanabe, T. Taniguchi, L. Fu, and L. Ju, Fractional quantum anomalous Hall effect in multilayer graphene, Nature (London) **626**, 759 (2024).

[31] J. Xie, Z. Huo, X. Lu, Z. Feng, Z. Zhang, W. Wang, Q. Yang, K. Watanabe, T. Taniguchi, K. Liu, *et al.*, Tunable fractional Chern insulators in rhombohedral graphene superlattices, Nat. Mater. **24**, 1042 (2025).

[32] A. P. Reddy, N. Paul, A. Abouelkomsan, and L. Fu, Non-Abelian fractionalization in topological minibands, Phys. Rev. Lett. **133**, 166503 (2024).

[33] M. Fujimoto, D. E. Parker, J. Dong, E. Khalaf, A. Vishwanath, and P. Ledwith, Higher vortexability: Zero-field realization of higher Landau levels, Phys. Rev. Lett. **134**, 106502 (2025).

[34] Z. Liu, B. Mera, M. Fujimoto, T. Ozawa, and J. Wang, Theory of generalized Landau levels and its implications for non-Abelian states, Phys. Rev. X **15**, 031019 (2025).

[35] F. C. Zhang and S. Das Sarma, Excitation gap in the fractional quantum Hall effect: Finite layer thickness corrections, Phys. Rev. B **33**, 2903(R) (1986).

[36] R. H. Morf, N. d'Ambrumenil, and S. Das Sarma, Excitation gaps in fractional quantum Hall states: An exact diagonalization study, Phys. Rev. B **66**, 075408 (2002).

[37] M. R. Peterson, T. Jolicoeur, and S. Das Sarma, Finite-layer thickness stabilizes the Pfaffian state for the 5/2 fractional quantum Hall effect: Wave function overlap and topological degeneracy, Phys. Rev. Lett. **101**, 016807 (2008).

[38] M. R. Peterson, T. Jolicoeur, and S. Das Sarma, Orbital Landau level dependence of the fractional quantum Hall effect in quasi-two-dimensional electron layers: Finite-thickness effects, Phys. Rev. B **78**, 155308 (2008).

[39] M. R. Peterson and S. Das Sarma, Quantum Hall phase diagram of half-filled bilayers in the lowest and the second orbital Landau levels: Abelian versus non-Abelian incompressible fractional quantum Hall states, Phys. Rev. B **81**, 165304 (2010).

[40] M. Storni, R. H. Morf, and S. Das Sarma, Fractional quantum Hall state at $\nu = \frac{5}{2}$ and the Moore-Read Pfaffian, Phys. Rev. Lett. **104**, 076803 (2010).

[41] Z. Papić, D. A. Abanin, Y. Barlas, and R. N. Bhatt, Tunable interactions and phase transitions in Dirac materials in a magnetic field, Phys. Rev. B **84**, 241306(R) (2011).
[42] Z. Papić, R. Thomale, and D. A. Abanin, Tunable electron interactions and fractional quantum Hall states in graphene, Phys. Rev. Lett. **107**, 176602 (2011).
[43] Z. Papić, D. A. Abanin, Y. Barlas, and R. N. Bhatt, Numerical studies of the fractional quantum Hall effect in systems with tunable interactions, J. Phys.: Conf. Ser. **402**, 012020 (2012).
[44] X. Wan, S. Sarkar, S.-Z. Lin, and K. Sun, Topological exact flat bands in two-dimensional materials under periodic strain, Phys. Rev. Lett. **130**, 216401 (2023).
[45] S. Sarkar, X. Wan, S.-Z. Lin, and K. Sun, Symmetry-based classification of exact flat bands in single and bilayer moiré systems, Phys. Rev. Lett. **135**, 016501 (2025).
[46] See Supplemental Material at http://link.aps.org/supplemental/10.1103/5yrq-qjkh for derivations of moiré flat-band wavefunctions, exact-diagonalization methods, Landau-level form factors and pseudopotentials, and additional analytical and numerical results on gap enhancement, Landau-level hybridization, and interaction screening.
[47] P. M. Eugenio and O. Vafek, Twisted-bilayer FeSe and the Fe-based superlattices, SciPost Phys. **15**, 081 (2023).
[48] S. Kharchev and A. Zabrodin, Theta vocabulary I, J. Geom. Phys. **94**, 19 (2015).
[49] J. K. Jain, *Composite Fermions* (Cambridge University Press, Cambridge, 2007).
[50] G. Murthy and R. Shankar, Hamiltonian theory of fractionally filled Chern bands, Phys. Rev. B **86**, 195146 (2012).
[51] M. O. Goerbig, R. Moessner, and B. Douçot, Electron interactions in graphene in a strong magnetic field, Phys. Rev. B **74**, 161407(R) (2006).
[52] I. Sodemann and A. H. MacDonald, Landau level mixing and the fractional quantum Hall effect, Phys. Rev. B **87**, 245425 (2013).
[53] C.-E. Ahn, W. Lee, K. Yananose, Y. Kim, and G. Y. Cho, Non-Abelian fractional quantum anomalous Hall states and first Landau level physics of the second moiré band of twisted bilayer $MoTe_2$, Phys. Rev. B **110**, L161109 (2024).
[54] X.-W. Zhang, C. Wang, X. Liu, Y. Fan, T. Cao, and D. Xiao, Polarization-driven band topology evolution in twisted $MoTe_2$ and WSe_2, Nat. Commun. **15**, 4223 (2024).
[55] F. Chen, W.-W. Luo, W. Zhu, and D. N. Sheng, Robust non-Abelian even-denominator fractional Chern insulator in twisted bilayer $MoTe_2$, Nat. Commun. **16**, 2115 (2025).
[56] J. Shi, J. Cano, and N. Morales-Durán, Effects of Berry curvature on ideal fractional Chern insulator many-body gaps, Phys. Rev. Res. **8**, L022045 (2026).
[57] D. Guerci, A. Abouelkomsan, and L. Fu, From fractionalization to chiral topological superconductivity in a flat Chern band, Phys. Rev. Lett. **135**, 186601 (2025).
[58] M. Yutushui, A. Dey, and D. F. Mross, Numerical case for identifying paired quantum Hall phases by their daughter states, Phys. Rev. Res. **8**, L022020 (2026).
[59] A. Vishwanath, Zero field fractional Hall states, now in graphene heterostructures, J. Club Condens. Matter Phys. (2023).
[60] G. W. Semenoff, Condensed-matter simulation of a three-dimensional anomaly, Phys. Rev. Lett. **53**, 2449 (1984).
[61] N. H. Shon and T. Ando, Quantum transport in two-dimensional graphite system, J. Phys. Soc. Jpn. **67**, 2421 (1998).
[62] C. Tőke, P. E. Lammert, V. H. Crespi, and J. K. Jain, Fractional quantum Hall effect in graphene, Phys. Rev. B **74**, 235417 (2006).
[63] F. D. M. Haldane, Fractional quantization of the Hall effect: A hierarchy of incompressible quantum fluid states, Phys. Rev. Lett. **51**, 605 (1983).
[64] S. A. Trugman and S. Kivelson, Exact results for the fractional quantum Hall effect with general interactions, Phys. Rev. B **31**, 5280 (1985).
[65] F. D. M. Haldane, in *The Quantum Hall Effect*, edited by R. E. Prange and S. M. Girvin (Springer, New York, 1987).
[66] J. Dong, J. Wang, P. J. Ledwith, A. Vishwanath, and D. E. Parker, Composite Fermi liquid at zero magnetic field in twisted $MoTe_2$, Phys. Rev. Lett. **131**, 136502 (2023).
[67] A. P. Reddy, F. Alsallom, Y. Zhang, T. Devakul, and L. Fu, Fractional quantum anomalous Hall states in twisted bilayer $MoTe_2$ and WSe_2, Phys. Rev. B **108**, 085117 (2023).
[68] C. Wang, X.-W. Zhang, X. Liu, Y. He, X. Xu, Y. Ran, T. Cao, and D. Xiao, Fractional Chern insulator in twisted bilayer $MoTe_2$, Phys. Rev. Lett. **132**, 036501 (2024).
[69] Y. H. Kwan, G. Wagner, J. Yu, A. K. Dagnino, Y. Jiang, X. Xu, B. A. Bernevig, T. Neupert, and N. Regnault, Regarding the existence of abelian fractional topological insulators in twisted $MoTe_2$ and related systems, Commun. Phys. **9**, 52 (2026).